

Multi-frame-based Cross-domain Image Denoising for Low-dose Computed Tomography

Yucheng Lu, Zhixin Xu, Moon Hyung Choi, Jimin Kim, and Seung-Won Jung

April 28, 2023

Abstract

Computed tomography (CT) has been used worldwide for decades as one of the most important non-invasive tests in assisting diagnosis. However, the ionizing nature of X-ray exposure raises concerns about potential health risks such as cancer. The desire for lower radiation dose has driven researchers to improve the reconstruction quality, especially by removing noise and artifacts. Although previous studies on low-dose computed tomography (LDCT) denoising have demonstrated the potential of learning-based methods, most of them were developed on the simulated data collected using Radon transform. However, the real-world scenario significantly differs from the simulation domain, and the joint optimization of denoising with modern CT image reconstruction pipeline is still missing. In this paper, for the commercially available third-generation multi-slice spiral CT scanners, we propose a two-stage method that better exploits the complete reconstruction pipeline for LDCT denoising across different domains. Our method makes good use of the high redundancy of both the multi-slice projections and the volumetric reconstructions while avoiding the collapse of information in conventional cascaded frameworks. The dedicated design also provides a clearer interpretation of the workflow. Through extensive evaluations, we demonstrate its superior performance against state-of-the-art methods.

Introduction

Computed tomography (CT) is one of the most widely used tools in clinical examinations nowadays due to its advantages of non-invasive and volumetric data acquisition. It allows us to restore piles of axial structures through reverse reconstruction, providing rich data representations that help access finer patterns for further evaluation and diagnosis.

Despite its great convenience and performance, there have been significant concerns about the potential health hazard to the patients. Especially, cell and organ damage may occur after CT scanning as a consequence of excessive exposure if proper measures against ionizing radiation are not considered. Even though the dosage of CT scanning is relatively low, exposure over a protracted time can still increase the risk of getting cancer [BH07]. Therefore, minimizing radiation exposure has been carried out with a sense of urgency in terms of both science and public opinion [BH07].

Since it is currently impractical to exclude CT from general health examinations, engineers have worked actively on reducing the radiation dosage applied to the subjects through various techniques, such as enlarging the field of view of the X-ray source, increasing the resolution of detector array both horizontally and vertically, improving the sensitivity of single detector unit, and increasing the table speed for faster scanning. All these efforts have led to considerable performance improvement over the past decades.

Besides hardware-based solutions, researchers have also paid attention to dosage reduction through software-assisted technology. Two representative methods are sparse-view CT, which uses a reduced number of projections per gantry rotation, and low-dose CT (LDCT), which uses a reduced intensity of the X-ray source. While the former tries to compensate for the artifacts introduced by the missing views, the latter gives rise to an image denoising problem, receiving more attention as similar tasks in other areas (*e.g.*, low-light image enhancement) have been extensively studied.

With the success of convolutional neural networks (CNNs) in low-level computer vision tasks, they have been rapidly adopted in medical imaging applications. Early studies have shown the impressive and promising performance of CNNs on LDCT denoising compared to conventional handcrafted regularizers [WGCM16, JMFU17, KMY17]. However, the protocol of LDCT denoising is significantly different from that of conventional image denoising, requiring further optimization to the obtained data representation (*i.e.*, projections) before the final reconstruction. Unfortunately, many existing works directly borrow the ideas from conventional image denoising and apply them to the reconstructed CT slices as a post-processing stage, which can be suboptimal for LDCT denoising. Although there are a few works in literature that handle projection data [WGCM16, YZL+19, LLZ+19, HWM20, ZHZ+21], they either operate on simulated 1D projection data which is not aligned with the modern CT scanner design or require considerable computation resource for end-to-end training. All the above limitations hinder these works from being more optimal and practical.

To tackle these problems, in this paper, we propose a two-stage denoising framework dedicated to LDCT data obtained from third-generation CT scanners. Specifically, at the first stage, a projection domain denoising network takes as input the successive projection slices and estimates sequential noise components, which are then rebinned and used by the image restoration network in the second stage for further refinement. This two-stage design takes the domain-specific characteristics into account while avoiding information degradation in common cascaded structures, yielding more satisfactory image quality both objectively and subjectively. In summary, the main contributions of this paper are as follows:

- We propose a two-stage framework for LDCT denoising. The proposed method is designed to work across both the projection domain and the image domain. It is specifically optimized for third-generation CT scanners, making it more efficient and practical.
- We model the noise and artifact properties of each stage based on the data acquisition process in the reconstruction pipeline. This design not only improves the denoising performance but also provides higher interpretation ability and transparency to end-users.
- We demonstrate through extensive experiments that our method significantly outperforms existing works both quantitatively and qualitatively.

The remaining sections of this paper are organized as follows: Section 2 reviews some existing works related to our topic and briefly discusses their limitations, Section 3 presents the proposed method in full detail, Section 4 provides the experiment setup and compares our results with the others from several representative works, and finally, Section 5 concludes the paper.

2 Related Works

Since the data acquisition and image restoration protocol of CT is different from that of conventional digital cameras, the design of the image denoiser can be highly flexible depending on the appearance of the data to be processed. Compared to early designs based on handcrafted image priors, some pioneering works [JMFU17, KMY17, CZK⁺17, WKEFL17] have shown the superior potential of CNNs in LDCT denoising. We thus mainly focus on CNN-based methods and classify most of the recent research into three categories, namely direct feed-forward image denoising, model-based iterative image reconstruction and denoising, and cross-domain joint optimization.

2.1 Direct Feed-forward Image Denoising

Direct feed-forward image denoising aims at removing noise directly from the reconstructed CT images in a single feed-forward manner, which can be formulated as

$$I_c = \mathcal{G}_I(I_n), \quad (1)$$

where I_n and I_c are the noisy input and the clean image processed by the denoiser \mathcal{G}_I , respectively. A significant merit of this approach is that it works in the 2D image domain as a post-processing step. With the provided low-dose and normal-dose image pairs, training becomes straightforward. Fan *et al.* [FSK⁺19] proposed a quadratic form of 2D convolution, achieving significant improvement. Zavala *et al.* [ZMRB⁺22] revisited the perfect reconstruction conditions of the encoder-decoder-structured CNNs with soft-shrinkage and proposed a learnable shrinkage layer to handle decomposed wavelet frames. Tao *et al.* [TWL⁺21] observed the specific patterns lying in the stacked view-by-view back-projection tensors and developed a CNN for these high-dimensional tensors. Zhang *et al.* [ZYL⁺21] designed a framework consisting of two parallel networks to handle the low-frequency and high-frequency components, where the popular and powerful Transformer architecture [VSP⁺17] was adopted as the network backbone.

When the ground-truth clean CT images are absent, generative adversarial learning could be a viable option for training CNNs: Shan *et al.* [SZY⁺18] employed 3D convolution in the design of the encoder-decoder network and supervised the transfer learning from a pre-trained 2D variant using the Wasserstein distance. Ghahermani *et al.* [GKST22] introduced an adversarial distortion learning method that considers the element-wise discrimination loss, reconstruction loss, pyramidal texture loss, and histogram loss in the supervision, leading to improved model generalization ability on datasets other than the one used for training. Zhang *et al.* [ZHS⁺21] employed an artifact and noise attention network to help improve the denoising performance and used an edge feature extraction path to compensate for the overly-smoothed details. Gu *et al.* [GY21] adopted the cycle consistency and proposed a model with adaptive instance normalization layers, achieving improved performance but with fewer parameters.

2.2 Iterative Image Reconstruction and Denoising

Although direct CT image denoising by a single feed-forward process is simple and fast, an obvious limitation is that the high-pass filter (*e.g.*, ramp filter) in the back-projection operation inevitably amplifies the noise component, which deteriorates the image denoising performance. To cope with this issue, an alternative is to apply model-based image reconstruction (MBIR), given as:

$$I_c = \arg \min_I \|\psi I - P_n\|_2^2 + \lambda \phi(I), \quad (2)$$

where ψ is the forward-projection operation that maps the reconstructed CT image I back to the projection domain, P_n represents the corresponding measurement, ϕ is a regularization function, and λ is a balancing parameter.

The solution of (2) is typically obtained in an iterative manner that updates the reconstructed image by comparing the forward-projection result to the measurement under some constraints. Many methods have been proposed to embed pre-trained CNN denoisers as a part of the update iteration for improved performance: Gupta *et al.*, [GJN⁺18] utilized a CNN to project the objective function onto the data manifold and proposed a relaxed version of the projected gradient descent method that guarantees the convergence of the optimization. Kang *et al.* [KCY⁺18] reviewed the denoising task under the low-rank Hankel structured matrix constraint and presented a wavelet residual network that learns to impose the low-rankness. Xia *et al.* [XLH⁺21] employed a learned graph convolutional network as an additional constraint to enhance nonlocal topological features in the low-dimensional patch manifold. He *et al.* [HYW⁺18] reformulated the problem as a dual-domain optimization task and modified the iteration of the alternating direction method of multipliers (ADMM) by using CNNs to represent the gradient, resulting in a parameterized plug-and-play ADMM optimization scheme. Chun *et al.* [CZLF19] introduced BCD-Net [CF18] for LDCT reconstruction and applied the accelerated proximal gradient method as the fast numerical solver. Ye *et al.* [YLM⁺21] took both the supervised regularization and the unsupervised regularization into account and proposed an optimization scheme to alternatively update the reconstruction result under specific constraints.

2.3 Cross-domain Joint Optimization

Besides MBIR methods, another solution with direct access to projection data is to apply denoising across different domains that cover the overall reconstruction pipeline, as follows:

$$I_c = \mathcal{G}_I(\varphi(\mathcal{G}_P(P_n))), \quad (3)$$

where \mathcal{G}_P and \mathcal{G}_I are denoisers on the projection domain and image domain, respectively. φ is a projection-to-image operation that can be performed by conventional reconstruction algorithms or learned models.

Several dedicated works fall under this category: Würfl *et al.* [WGCM16] utilized a multi-layer perceptron to model the behavior of filtering, back-projection, and non-negative constraint for sinogram-to-image reconstruction. Unal *et al.* [UEY21] presented a training protocol without the need for ground-truth clean images, where the J-invariant principle is employed to enable self-supervision. Li *et al.* [LLZ⁺19] designed a model named iCT-Net with the FBP operation replaced by a novel back-projection layer. He *et al.* [HWM20] presented a deep learning-based Radon inversion framework, where the filtered sinogram is resampled by a sinusoidal back-projection layer. Zhang *et al.* [ZIL⁺21] adopted the Fourier feature representation in their proposed sinogram prediction module and designed an iterative optimization scheme via forward and backward projection. Another work [ZHZ⁺21] combined two 3D ResUNets for the projection domain and image domain denoising and trained them using cross-domain supervision and adversarial learning.

The aforementioned methods have contributed to LDCT denoising to some extent, however, there is room for improvement: For image domain denoising, lacking direct access to the projection data increases difficulties in distinguishing between subtle structures and weak noised-induced artifacts. For MBIR-based methods, the simulated parallel scanner geometry is not aligned with modern multi-slice spiral design, fitting it to the actual gantry geometry will likely introduce extra complexity to the optimization or even affect the convergence. As to cross-domain frameworks, previous cascaded models suffer from the overly-smoothing issue when trained individually, while attempts at end-to-end fine-tuning become challenging due to the huge amount of data required for a complete reconstruction.

Unlike the existing works, our proposed framework takes the full characteristics of the CT image reconstruction pipeline into account and performs joint projection domain denoising and image domain refinement while avoiding the complexity and difficulty of end-to-end fine-tuning without compromised performance observed in other cascaded designs. To the best of our knowledge, there are only very few works closely related to ours in literature: Yin *et al.* [YZL⁺19] proposed a framework containing two 3D sub-networks for sinogram and image denoising, respectively, where each sub-network was trained separately to take as input volumetric frames and estimate noise using 3D convolutions. However, this cascaded design still struggles to recover from aggressive denoising. Also, the effect of rebinning has not been considered. As a result, performance improvement is limited. In comparison, our method decomposes the reconstruction pipeline into several learning-based optimization problems

according to the characteristics of data representation, which yields more transparency and higher interpretation ability, thus strengthening the system’s robustness subject to different gantry geometries.

3 Proposed Method

In this section, we first discuss the intuition behind the design and offer the readers a brief overview. We then provide more details of the proposed framework.

3.1 Reconstruction Revisit

Pixels in CT projection are obtained through the line integrals along the attenuating path. Without considering other effects (*e.g.*, beam hardening), the ideal clean measurement p_c is given as:

$$p_c = -\ln\left(\frac{N}{N_0}\right), \quad (4)$$

where N_0 and N are the incident and received intensity, respectively. However, noise is inevitable due to the quantum effects of photons. According to [WME⁺06], the measurement under clinical environment, denoted as p_n , can be approximated by:

$$p_n = p_c + \frac{X}{\sqrt{N_0 \exp(-p_c)}}, \quad (5)$$

where $X \sim \mathcal{N}(0, 1)$ is a unit Gaussian random variable. In addition, each measurement in the detector array is further parameterized by two extra variables to represent the spatial information of the ray, namely the ray distance d to the isocenter and the ray angle α to the table. Hence, the observed data representation is given as $p_n = P_n(d, \alpha)$.

Modern CT scanners usually perform scanning with helical trajectories, which requires an additional step called rebinning to convert raw projections to pseudo-parallel geometry via the following slicing operation:

$$\hat{P}_n(i) = P_n(d_i, \alpha_i), \quad (6)$$

where i is an element index in the rebined projection data. As the slicing indices are usually fractions, this operation is basically a 2D interpolation.

After that, all the resulting projections are transformed into image representation through CT reconstruction methods, where FBP is a popular choice. Without considering the multi-slice geometry, FBP can be briefly described as:

$$I_n(u, v) = \frac{\pi}{M} \sum_{m=1}^M \hat{P}_n(u \cos \theta_m + v \sin \theta_m), \quad (7)$$

where (u, v) denotes the pixel location, \hat{P} represents the filtered result of \hat{P} , θ_m is the m -th projection angle, and M is the number of rebined projections. Readers are referred to [Hsi03] for more details regarding the whole reconstruction pipeline.

Conventional images captured by camera sensors are pixel-wise uncorrelated in noise. Unfortunately, CT images do not inherit such properties because the reconstruction consists of several steps of taking non-linear weighted averages of neighboring data. Worse still, elements in projections contribute differently to the reconstruction due to the helical trajectory of the scanner. Last but not least, automatic gain control (AGC) is widely utilized to reduce excessive exposure, which results in inconsistent noise levels among projections from the same study, as the values reflect the material attenuation rather than the ray intensity. Most existing works, summarized in Sections 2.1, 2.2, and 2.3, did not consider these limitations, leading to unsatisfactory performance.

3.2 Framework Overview

An overview of the proposed framework is presented in Fig. 1. It mainly performs the projection domain denoising and the image domain refinement, embodied by multi-frame-based neural networks, named MPD-Net and MIR-Net, respectively.

Let $S_{n*}^P = [P_{n*}^1, P_{n*}^2, \dots, P_{n*}^K]$ denote a sequence of K consecutive noisy projections, where $* \in \{l, r\}$ denotes the left or the right candidate to be sampled in (6), and the upper-script represents the time step, which can be omitted when unnecessary. Given S_{n*}^P as the input, MPD-Net performs multi-frame noise estimation using a sliding window of size $2F + 1$ for every projection, resulting in a clean sequence $S_{c*}^P = [P_{c*}^{F+1}, P_{c*}^{F+2}, \dots, P_{c*}^{K-F}]$, as follows:

$$\begin{aligned} P_{c*}^t &= P_{n*}^t + R^t \\ &= P_{n*}^t + \mathcal{G}_{MPD}(P_{n*}^{t-F}, \dots, P_{n*}^t, \dots, P_{n*}^{t+F}), \end{aligned} \quad (8)$$

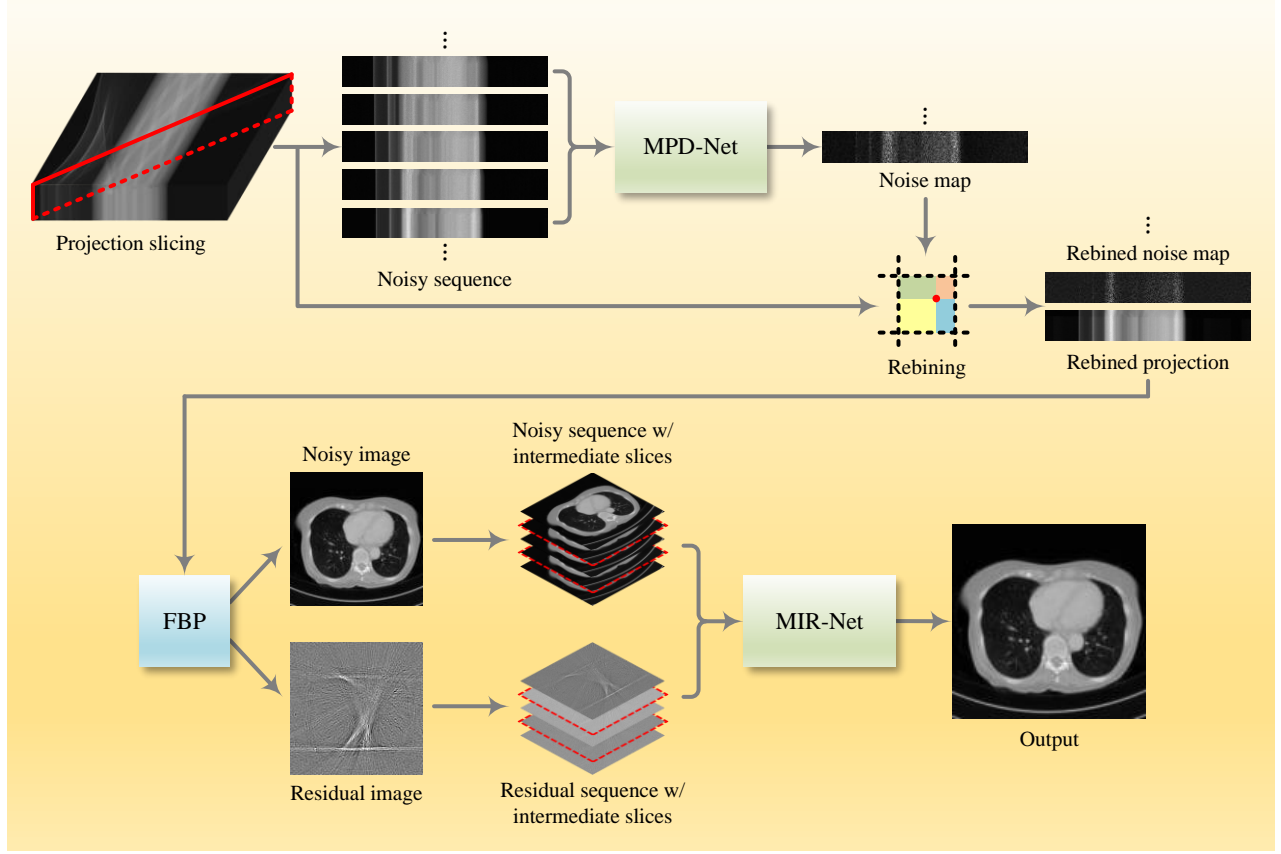


Figure 1: Overview of the proposed multi-stage hierarchical framework. The curly brackets indicate the concatenation operation. Note that only a single stream is shown in the projection domain denoising, and all the noise components are amplified for better visibility.

where \mathcal{G}_{MPD} represents MPD-Net, R_*^t represents its output, $t \in \{F+1, F+2, \dots, K-F\}$, and $K \gg F$.

The rebined projection sequence, denoted as $\hat{S}_c^P = [\hat{P}_c^{F+1}, \hat{P}_c^{F+2}, \dots, \hat{P}_c^{K-F}]$, is then obtained by the weighted summation over adjacent projections as follows:

$$\hat{P}_c^t = \omega_{00}P_{cl}^t + \omega_{01}P_{cr}^t + \omega_{10}P_{cl}^{t+1} + \omega_{11}P_{cr}^{t+1}, \quad (9)$$

where ω_{00} , ω_{01} , ω_{10} , and ω_{11} are interpolation weights that add up to one.

After that, the conjugate projections with projections angles $\theta_j = \theta_j + k\pi$ are filtered and back-projected onto a 2D plane, forming a back-projection view V_{θ_j} as follows:

$$V_{\theta_j}^z(u, v) = \frac{1}{H_{\theta_j}} \sum_k h(z_{j,k} - z) \hat{P}_c(u \cos \theta_j + v \sin \theta_j), \quad (10)$$

where $z_{j,k} - z$ is the axial offset of the ray to the reconstruction center z , h is a non-linear weighting function related to the multi-slice spiral geometry, and H_{θ_j} is given by:

$$H_{\theta_j} = \sum_k h(z_{j,k} - z). \quad (11)$$

A complete reconstruction can then be derived once a half-turn L is reached:

$$I_c^z(u, v) = \frac{\pi}{L} \sum_{j=1}^L V_{\theta_j}^z(u, v). \quad (12)$$

Similar to the projection domain denoising, when a sequence of Q reconstructed images is collected, MIR-Net takes the sequence $S_c^I = [I_c^{z_1}, I_c^{z_2}, \dots, I_c^{z_Q}]$ as the input and generates the refined image as the final result using a sliding window of size $2F+1$, given as:

$$\begin{aligned}
I_r^{zi} &= I_c^{zq} + R_r^{zq} \\
&= I_c^z + \mathcal{G}_{MIR}(I_c^{zq-F}, \dots, I_c^{zq}, \dots, I_c^{zq+F})
\end{aligned} \tag{13}$$

where \mathcal{G}_{MIR} represents MIR-Net, R_r^{zq} is its output, and $q \in \{F+1, F+2, \dots, Q-F\}$. Different from MPD-Net, the input to MIR-Net has a stride of $F+1$, *i.e.*, $q \pmod{F+1} \equiv 1$, which will be explained later.

3.3 Multi-frame-based Projection Denoising

We observe that modern scanners with multi-slice detector geometry provide inter-slice (*i.e.*, *detector array*) and intra-slice (*i.e.*, *sinogram*) redundancy that are both beneficial for denoising. As can be seen from the example shown in Fig. 2, the inter-slice similarity provides the projected structural details of the objects, while the intra-slice similarity presents the relative motion between objects. Based on this observation, unlike existing methods that directly operate on 2D sinograms, we take both the inter-slice and the intra-slice redundancy into account. As discussed Sec. 3.1, the dominant source of noise is the photon noise that follows a Poisson distribution. We thus consider reformulating the task as a burst imaging denoising problem and propose MPD-Net to capture both the inter-slice and intra-slice features.

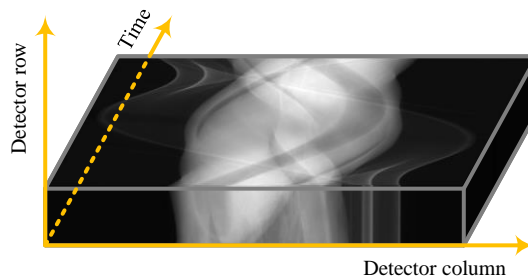


Figure 2: A sample clip from the raw projections obtained by a third-generation multi-slice scanner.

The main structure of MPD-Net is depicted in Fig. 4(a). Inspired by [TDV20], a multi-step denoising structure consisting of two modified residual U-Nets (ResUNets) is adopted. Each ResUNet takes $2F+1$ frames as the input and predicts a clean version of the middle frame via residual learning. Different from the original design in [TDV20] where the middle frame is denoised twice while the same noise prior is reused at the second step, we take the predicted residual from the first step along with the untouched frames as the input of the second step to avoid potential accumulated artifacts. Furthermore, the adaptive mix-up [WQL+21] is also employed as we empirically find it useful in boosting performance.

The design based on the above intuition could be sub-optimal since the rebinning operation in (6) generates pseudo-parallel projections that are obtained across time. Besides, some scanners apply the flying focal spot technique to improve axial resolution, where the rebinning process comes with another step that interleaves rebinned rows from two focal spots. All these cross-time and cross-focal-spot operations lead to broken inter-slice correlations along detector channels. As we will demonstrate in Section 4.2, applying rebinning after the denoising process results in unsmooth projections due to the absence of long-term consistency. However, if rebinning is performed before the denoising process, as it is essentially an interpolation operation, the element-wise noise independence will be violated, which is undesirable.

To cope with this issue, we decompose the rebinning process into two operations, namely integer slicing and weighted summation, and relocate MPD-Net in between the two operations. The integer slicing extracts four untouched neighbors from raw projections, while the weighted summation performs rebinning to the denoised results. This simple trick not only retains both the noise property and inter-slice smoothness but also avoids complicated long-term memory mechanisms in the network.

It is worth noticing that MPD-Net works seamlessly over time using a sliding window. Moreover, unlike conventional cameras, the measurement in (4) represents the attenuation ratio rather than the ray intensity, which does not reflect the properties of photon noise. As shown in Fig. 3, when AGC is enabled, which is the default setting in clinical exams [Hsi03], the noise level varies among projections and scanning locations. Therefore, blind denoisers tend to learn a more aggressive strategy that discards subtle but useful details if this characteristic is not explicitly handled. Hence, we concatenate information of the X-ray source intensity to the input and train MPD-Net as a non-blind denoiser to obtain better performance.

3.4 Multi-frame-based Image Refinement

Although the proposed MPD-Net can significantly reduce the noise of multi-slice projections, it is still far from being satisfactory for two reasons. First, MPD-Net does not capture the structural features of the final reconstructed image because

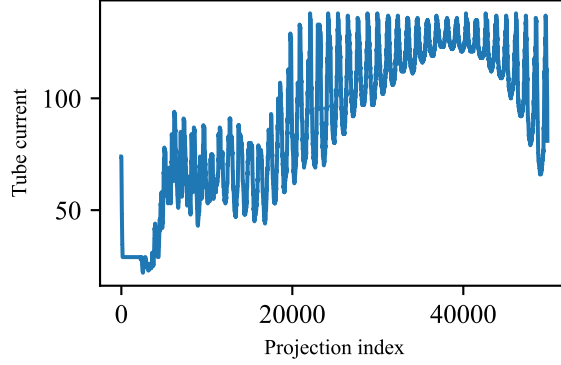


Figure 3: X-ray tube current vs. projection index with AGC enabled. It directly reflects the amount of source photon noise fluctuating during the full scan.

the reconstruction plane is in parallel with the ray trajectory. Second, the remaining noise in the results might lead to streak artifacts during FBP reconstruction due to the usage of a high-pass filter. To tackle these problems, we introduce a second network (*i.e.*, MIR-Net) to further refine the LDCT image.

Fig. 4(b) presents the structure of MIR-Net, consisting of a single ResUNet. MIR-Net takes the reconstructed CT image sequence S_c^I as the input and produces the residual R_r as the output. The hourglass design enables an expanding receptive field that better captures structural features without large kernels, where we observe greater performance against other straight shape-preserving designs.

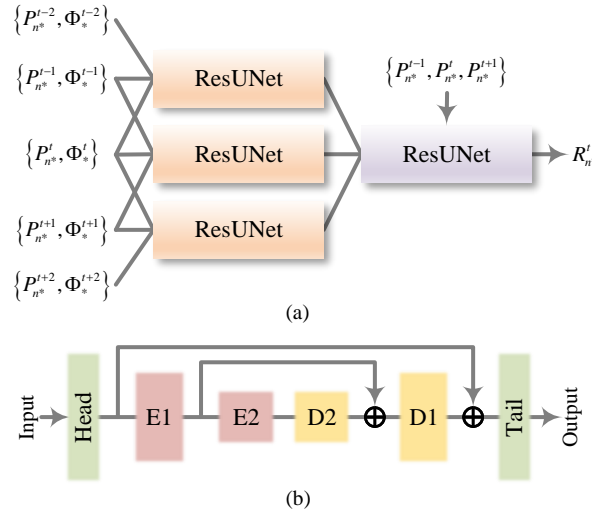


Figure 4: Network details: (a) MPD-Net with $F=1$, where ResUNets with different colors represent networks with individual parameters. Φ is the X-ray source intensity; (b) the structure of MIR-Net and ResUNet, where E1-E2 represent encoding blocks, and D1-D2 represent decoding blocks.

As the analysis based on burst imaging is rational in modeling the behavior of MPD-Net in the projection domain, it is intuitive to extend the same principles to MIR-Net in the image domain. However, we believe that this is not the case. In the projection domain, projections are acquired by line integrals through a 3D volume of the object, and the successive projections can be viewed as observations of the same object from slightly different viewpoints. Therefore, MPD-Net works as a video denoiser that implicitly handle parallax, including occlusion and motion compensation. Unfortunately, the reconstructed CT images do not share such properties: In the image domain, a CT image is actually a 3D slice orthogonal to the detector array. Let I^{z_q} and $I^{z_{q+1}}$ be two consecutive CT images, respectively, and D be the slice thickness. As can be seen in Fig. 5(a), when $|z_{q+1} - z_q| > D$, the (ideal) reconstructed CT images do not share features between slices, meaning that redundant observations are no longer available for further refinement.

We propose a simple yet effective approach to tackle this issue by introducing overlapped slices as intermediate representations.

According to (10), the reconstructed CT image centered at location z is obtained by averaging nearby back-projections through a weighting function h . We refer to the reconstruction method in [SRB⁺04], where h is given as:

$$h(\Delta z) = \max\left(0, 1 - \frac{|\Delta z|}{D}\right) w(r), \quad (14)$$

where r denotes the detector row index, and $\Delta z = |z_{q+1} - z_q|$ represents the distance between the projection and the reconstruction center along the table direction.

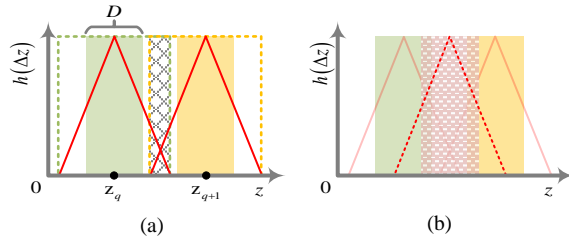


Figure 5: Illustration of slice relations: (a) a pair of non-overlapped slices when $\Delta z > D$, the dotted boxes are their projection data grabbing range, the red lines are corresponding weights that contribute to h (w/o $w(r)$), and the grid in between indicates shared projections; (b) the proposed multi-slice redundancy ($F = 1$).

Without considering the effect of the second term $w(r)$ [SRB⁺04], the amount of projection data required for a complete reconstruction, defined by $h(\Delta z) > 0$, simply lies in $(z - D, z + D)$, indicating that the expansion of required projections is wider than the slice thickness. In other words, there may still be a small number of shared projections used in reconstructing both I^z and I^{z+1} . These shared features enable the multi-frame refinement by MIR-Net in a more interpretable way based on the principles of burst imaging. As Fig. 5(a) shows, the weights of shared projections become rather insignificant as Δz increases; one could insert more slices in between to better utilize these weak features. To this end, we reconstruct F slices as intermediate observations between each pair of adjacent slices and collect $2F + 1$ images as the input to MIR-Net. Fig. 5(b) presents the proposed solution when $F = 1$; by doing so, the intermediate projections can be emphasized, thus providing a strong reference for further refinement. It is worth mentioning that these intermediate representations cannot be obtained via linear interpolation from adjacent slices as the weighting function is non-linear.

Besides, we notice a certain degree of degradation in the final results due to the aggressive denoising in individual sub-network, which commonly occurs in cascaded networks. A simple method to alleviate this issue is to fine-tune the entire chain in an end-to-end manner. However, as discussed in Section 2, end-to-end training is expensive and impractical. Alternatively, to compensate for the aggressive denoising of MPD-Net, rather than obtaining the processed projections from MPD-Net by (8), we use their concatenation form $[P_{n*}^t, R_*^t]$ such that the subtle details in the original noisy projections can be well preserved. Note that (9)-(12) apply linear operations, so P_{n*}^t and R_*^t can be processed independently before feeding into MIR-Net. In short, the image domain refinement defined in (13) is rewritten as follows:

$$\begin{aligned} I_r^{z_q} &= I_n^{z_q} + R_r^{z_q} \\ &= I_n^z + \mathcal{G}_{MIR}\left(\hat{I}_c^{z_{q-F}}, \dots, \hat{I}_c^{z_q}, \dots, \hat{I}_c^{z_{q+F}}\right), \end{aligned} \quad (15)$$

where $\hat{I}_c^{z_q} = [I_n^{z_q}, R_c^{z_q}]$ is the concatenation of the noisy image $I_n^{z_q}$ and the residual $R_c^{z_q}$ reconstructed using the raw projections and MPD-Net predictions, respectively.

4 Experiments and Analysis

In this section, we first provide implementation details and some ablation studies to verify our design. Then, we evaluate its performance both quantitatively and qualitatively.

4.1 Implementation Details

The proposed framework was implemented in PyTorch and trained on an RTX 3090 GPU. We chose Adam optimizer to update model parameters¹. 49 abdomen CT scans, collected by a Siemens SOMATOM Definition Flash CT scanner from the

¹Code available at <https://github.com/YCL92/TMD-LDCT>

Low Dose CT Image and Projection Data V4 [MCHI+21], were used as the dataset for training, validation, and testing. Among them, 19 scans aligned with the 2016 Low-dose CT AAPM Grand Challenge [oPiM16] were selected as the testing dataset. The detailed data partitions are given in Table 1. We followed the methods described in [FSU+05, SRB+04] for rebinning, filtering, back-projection, and weighted summation, where the Shepp–Logan filter was chosen as the reconstruction kernel, and the slice thickness from metadata was used.

Table 1: Dataset Partition Summary

| Partition | Scan ID |
|------------|------------------------------------------|
| Training | L004, L006, L019, L033, L057, L064, L071 |
| | L072, L077, L081, L107, L110, L114, L116 |
| | L125, L131, L134, L150, L160, L170, L175 |
| | L178, L179, L193, L203, L210, L212, L220 |
| | L221, L229, L232, L237, L248, L273, L299 |
| Validation | L148 |
| Testing | L014, L056, L058, L075, L123, L145, L186 |
| | L187, L209, L219, L241, L266, L277 |

During the network training, we used only L1 loss to supervise both MPD-Net and MIR-Net. The initial learning rate was set to 1×10^{-4} , which was then reduced to 1×10^{-5} if the model performance on the validation set has no further improvement after certain steps. The full convergence of the two CNNs took about 30 and 100 epochs, respectively.

Table 2: Validation Results of Ablation Studies

| Index | Description | PSNR | Comment |
|-------|--------------------|-------|----------------|
| - | Reference | 27.29 | Full framework |
| 1 | w/o MPD-Net | 27.16 | - |
| 2 | w/o MIR-Net | 26.56 | - |
| 3 | w/o noise quanta | 26.41 | w/o MIR-Net |
| 4 | Pre-denoising | 26.33 | w/o MIR-Net |
| 5 | Summed input | 27.11 | - |
| 6 | Single-frame input | 27.20 | - |

4.2 Ablation Studies

We conducted several ablation studies to show the effectiveness of the proposed framework:

1. Two studies were performed to evaluate the individual contribution of MPD-Net and MIR-Net.
2. In Section 3.3, the relation between the pixel values and the X-Ray noise quanta was discussed. To verify this, we trained another MPD-Net without the source intensity information (*i.e.* noise quanta) as the complementary channel to the input.
3. In Section 3.3, the effect of rebinning was also analyzed; we thus performed another study to prove our hypothesis. Specifically, we placed MPD-Net as a pre-processing module before the rebinning operation.
4. We verified the effectiveness of concatenating noisy and residual reconstruction images by directly feeding the summed result as the input to MIR-Net.
5. We reduced the number of input frames to only one and performed another study to verify the effect of multi-frame inputs.

The ablation studies were conducted on the validation set; we reported the measured PSNRs in Table 2. Note that the display window for the reconstructed images was set to [30, 400]. It can be seen that both MPD-Net and MIR-Net played important roles in enhancing the reconstruction quality of LDCT. For MPD-Net, introducing the noise prior (*source intensity*) led to

quality improvement while placing the model before the rebinning operation resulted in sub-optimized performance. Similarly, it is noticed that the summation in (8) affected the reconstruction, mostly due to aggressive denoising. Also, volumetric input brought extra benefits to MIR-Net. All these ablation studies were well aligned with our aforementioned hypothesis and analysis.

4.3 Objective Evaluation

We conducted an objective evaluation to compare the proposed framework with nine state-of-the-art methods, namely RED-CNN [CZK+17], WGAN [YYZ+18], CPCE-3D [SZY+18], QAE [FSK+19], DP-ResNet [YZL+19], EDCNN [LJLW20], TransCT [ZYL+21], DU-GAN [HZS21], and CTformer [WFW+22]. We retrained all these methods using our training set for a fair comparison. Specifically, as the overall volume of the training set differs from the original ones, we retrained each model with more iterations and terminated when the validation performance saturated. We employed the PSNR and structural similarity (SSIM) as the quantitative evaluation metrics and used the display windows stored in the image metadata during the evaluation. The results are shown in Tables 3 and 4.

Table 3: Objective Evaluation Results on the Test Set (PSNR)

| | L014 | L056 | L058 | L075 | L123 | L145 | L186 | L187 | L209 | L219 | L241 | L266 | L277 |
|-------------|--------------|--------------|--------------|--------------|--------------|--------------|--------------|--------------|--------------|--------------|--------------|--------------|--------------|
| Low-dose CT | 24.48 | 23.52 | 20.23 | 24.15 | 23.37 | 22.86 | 23.16 | 23.22 | 22.70 | 22.37 | 19.84 | 27.60 | 20.36 |
| RED-CNN | 28.77 | 28.18 | 25.45 | 28.44 | 28.20 | 28.11 | 28.27 | 28.06 | 27.71 | 27.33 | 25.49 | 33.41 | 25.55 |
| WGAN | 25.57 | 25.34 | 23.04 | 25.91 | 25.30 | 25.54 | 25.79 | 25.51 | 24.47 | 24.78 | 23.25 | 30.73 | 23.28 |
| CPCE-3D | 26.71 | 26.08 | 23.38 | 26.72 | 26.13 | 26.04 | 26.43 | 26.19 | 25.49 | 25.40 | 23.50 | 31.23 | 23.58 |
| QAE | 28.45 | 27.81 | 24.97 | 28.17 | 27.74 | 27.72 | 27.98 | 27.58 | 27.31 | 26.92 | 25.16 | 33.06 | 25.19 |
| DP-ResNet | 27.68 | 27.38 | 25.14 | 27.39 | 27.39 | 27.61 | 27.52 | 27.39 | 26.79 | 26.63 | 24.95 | 32.71 | 24.98 |
| EDCNN | 28.56 | 27.81 | 25.15 | 28.23 | 27.88 | 27.72 | 28.03 | 27.68 | 27.41 | 27.02 | 25.23 | 33.27 | 25.27 |
| TransCT | 28.01 | 27.57 | 24.98 | 27.79 | 27.58 | 27.66 | 27.67 | 27.60 | 27.00 | 26.87 | 25.03 | 32.13 | 25.08 |
| DU-GAN | 27.53 | 27.04 | 24.42 | 27.45 | 27.16 | 26.96 | 27.19 | 27.21 | 26.47 | 26.30 | 24.56 | 31.73 | 24.58 |
| CTformer | 28.16 | 27.48 | 24.58 | 27.92 | 27.51 | 27.39 | 27.70 | 27.41 | 26.93 | 26.70 | 24.90 | 32.65 | 24.80 |
| Ours | 29.03 | 28.66 | 26.15 | 28.71 | 28.52 | 28.47 | 28.63 | 28.45 | 28.06 | 27.69 | 25.80 | 33.81 | 25.95 |

Table 4: Objective Evaluation Results on the Test Set (SSIM)

| | L014 | L056 | L058 | L075 | L123 | L145 | L186 | L187 | L209 | L219 | L241 | L266 | L277 |
|-------------|---------------|---------------|---------------|---------------|---------------|---------------|---------------|---------------|---------------|---------------|---------------|---------------|---------------|
| Low-dose CT | 0.7956 | 0.7430 | 0.6695 | 0.7711 | 0.7462 | 0.7006 | 0.7162 | 0.7279 | 0.7446 | 0.7014 | 0.6281 | 0.7780 | 0.6567 |
| RED-CNN | 0.8905 | 0.8772 | 0.8189 | 0.8762 | 0.8727 | 0.8591 | 0.8650 | 0.8650 | 0.8729 | 0.8448 | 0.7948 | 0.8858 | 0.8171 |
| WGAN | 0.8548 | 0.8351 | 0.7649 | 0.8375 | 0.8229 | 0.8000 | 0.8018 | 0.8101 | 0.8184 | 0.7940 | 0.7336 | 0.8537 | 0.7570 |
| CPCE-3D | 0.8685 | 0.8372 | 0.7748 | 0.8521 | 0.8395 | 0.8162 | 0.8364 | 0.8279 | 0.8397 | 0.8059 | 0.7621 | 0.8611 | 0.7804 |
| QAE | 0.8892 | 0.8721 | 0.8110 | 0.8740 | 0.8682 | 0.8527 | 0.8636 | 0.8565 | 0.8702 | 0.8386 | 0.7953 | 0.8868 | 0.8149 |
| DP-ResNet | 0.8750 | 0.8673 | 0.8113 | 0.8571 | 0.8584 | 0.8489 | 0.8473 | 0.8512 | 0.8590 | 0.8293 | 0.7675 | 0.8733 | 0.7993 |
| EDCNN | 0.8887 | 0.8678 | 0.8135 | 0.8738 | 0.8678 | 0.8512 | 0.8655 | 0.8578 | 0.8692 | 0.8388 | 0.7975 | 0.8884 | 0.8165 |
| TransCT | 0.8784 | 0.8668 | 0.8039 | 0.8639 | 0.8616 | 0.8494 | 0.8521 | 0.8549 | 0.8608 | 0.8330 | 0.7745 | 0.8675 | 0.8047 |
| DU-GAN | 0.8736 | 0.8565 | 0.7937 | 0.8596 | 0.8538 | 0.8312 | 0.8404 | 0.8468 | 0.8504 | 0.8244 | 0.7739 | 0.8610 | 0.7958 |
| CTformer | 0.8843 | 0.8666 | 0.8020 | 0.8693 | 0.8629 | 0.8475 | 0.8576 | 0.8536 | 0.8637 | 0.8339 | 0.7860 | 0.8799 | 0.8066 |
| Ours | 0.8938 | 0.8845 | 0.8349 | 0.8803 | 0.8778 | 0.8663 | 0.8727 | 0.8708 | 0.8789 | 0.8512 | 0.8032 | 0.8937 | 0.8263 |

The proposed framework outperformed other state-of-the-art methods by a significant margin in all 13 studies in terms of both PSNR and SSIM, indicating its superiority. To visually compare the image quality, we selected two representative sample slices, as shown in Figs. 6-7.

Fig. 6 is a challenging example of a high-density lesion identified as metastatic cholangiocarcinoma. All methods were able to suppress the noise in LDCT data to some extent and improve the visibility of the lesion area. However, some methods, such as RED-CNN and DP-ResNet, suffered from the over-smoothing problem, while GAN-based methods, such as WGAN and DU-GAN, or some perceptual loss-based methods, such as CPCE-3D, did not perform well in the denoising task. In comparison, our method not only removed most of the noise but also reserved sharpness in the lesion area, reaching a satisfactory balance between noise and details.

In Fig. 7, we reveal the ability of detail preservation by identifying the right portal and hepatic veins. It is obvious that both the shape of the right portal vein and the margin visibility of the right hepatic vein were well-preserved in our result. By contrast, other methods either failed to preserve shapes and edges or mistakenly smoothed out subtle patterns, making these images less reliable in medical applications.

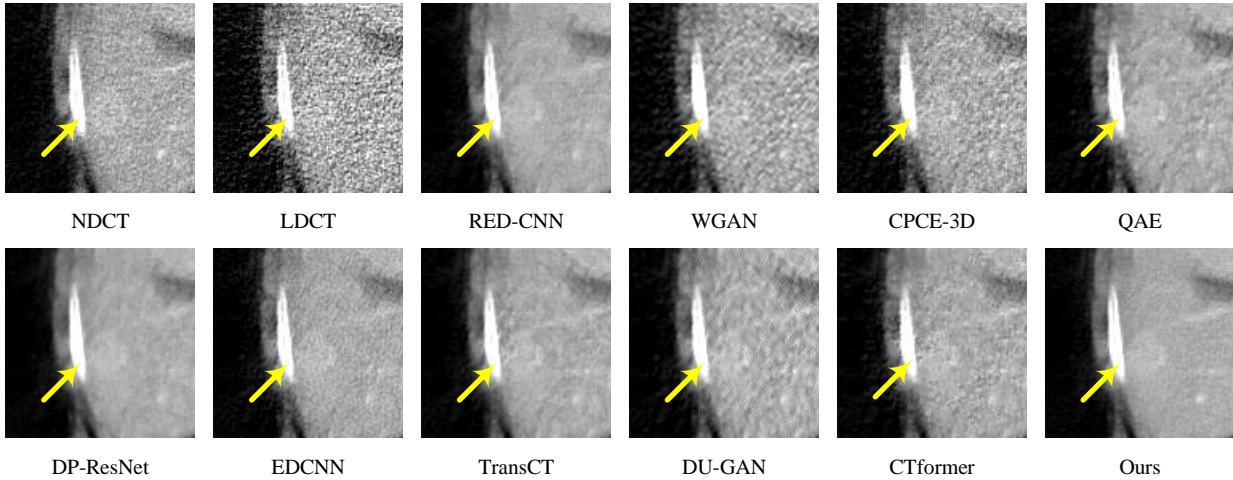


Figure 6: Clinical sample from slice ID L241-029. The high-density lesion (metastatic cholangiocarcinoma) is marked by the yellow arrow (WC: 40, WW: 300).

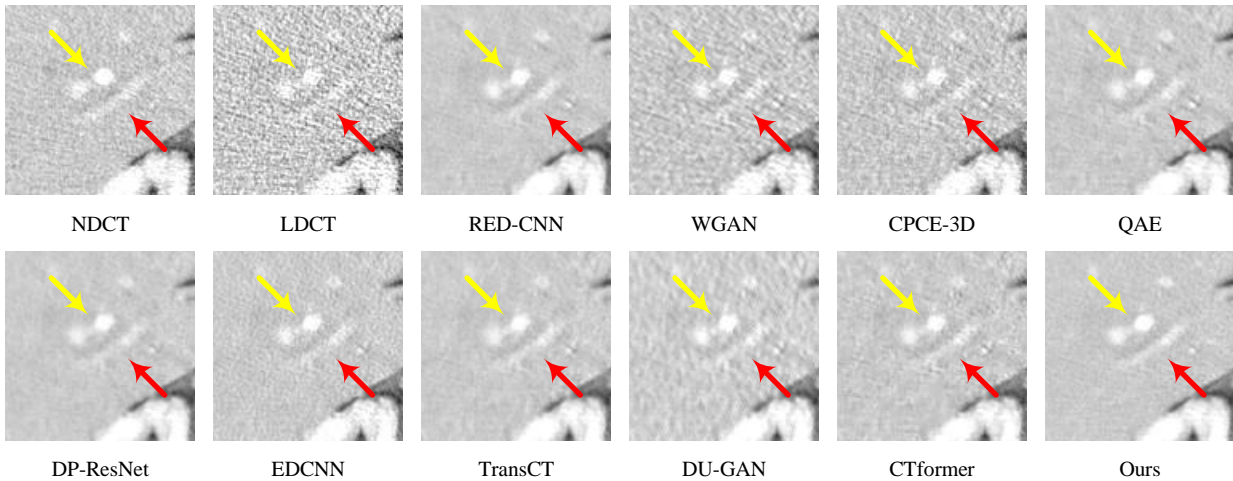


Figure 7: Clinical sample from slice ID L219-045. The right portal and hepatic veins are marked by the yellow and red arrows, respectively (WC: 40, WW: 300).

4.4 Subjective Test

Although the quantitative evaluation shows significant improvement of the proposed framework against other methods, the quantitative metrics might not reflect the real-world perceptual quality of the human visual system. In other words, a professional radiologist might pay special attention to certain aspects when reviewing CT images. As the main application of CT is to assist clinical diagnosis, the true value should be evaluated by medical experts. To this end, two radiologists with clinical experience of 12 years and 9 years, respectively, were invited to perform a subjective evaluation. During the test, three images, including a normal-dose CT, a low-dose CT, and a processed low-dose CT, were shown to the reviewer. For each study, the reviewers were requested to evaluate the perceptual quality of all candidates and assign scores with respect to noise suppression, contrast retention, margin sharpness, and diagnostic acceptability, respectively. A five-point scale table was employed, where the lowest score (*i.e.*, 1) was assigned to the low-dose CT while the highest score (*i.e.*, 5) was assigned to the normal-dose CT as the gold standard. The indices of ten candidates were shuffled for each study to avoid biased judgments.

The subjective evaluation results are summarized in Table 5. It can be seen that the proposed method received the highest scores against other candidates by a significant margin in all aspects, which is well-aligned with the results from the objective evaluation. Interestingly, when it comes to noise suppression and margin sharpness, they often behave inversely due to aggressive denoising, which explains the large margins in the results of RED-CNN, DP-ResNet, and TransCT, while the introduction of detail preservation constraints (*e.g.*, perceptual loss in CPCE-3D and adversarial loss in WGAN) may lead to compromised denoising performance. Once again, the proposed method is able to reach a pleasing balance between these aspects, yielding

Table 5: Subjective Evaluation Results on the Whole Test Set

| | RED-CNN | WGAN | CPCE-3D | QAE | DP-ResNet | EDCNN | TransCT | DU-GAN | CTformer | Ours |
|--------------------------|---------|------|---------|------|-----------|-------|---------|--------|----------|-------------|
| Noise suppression | 4.38 | 3.08 | 3.19 | 3.65 | 4.38 | 4.15 | 4.35 | 3.31 | 3.69 | 4.62 |
| Contrast retention | 3.88 | 3.77 | 3.96 | 3.73 | 3.42 | 4.15 | 3.62 | 4.12 | 3.85 | 4.46 |
| Margin sharpness | 2.65 | 2.85 | 2.81 | 2.58 | 2.46 | 2.73 | 2.46 | 2.69 | 2.54 | 3.38 |
| Diagnostic acceptability | 3.58 | 3.31 | 3.58 | 3.31 | 3.73 | 3.81 | 3.50 | 3.46 | 3.35 | 4.19 |

satisfactory results that specialists prefer. In short, the proposed framework can remove noise and reconstruction artifacts from LDCT data while preserving sufficient details with satisfactory clearness and sharpness.

5 Conclusions

The main goal of this paper is to improve the quality of LDCT images for multi-slice spiral CT. We provided a comprehensive discussion of the proposed two-stage processing pipeline across both the projection domain and the image domain and analyzed the impacts of rebinning and filtered back-projection to the final reconstruction. To fully utilize the inter-slice and intra-slice similarity inherent in the acquired projection volume, we transformed the task into a multi-frame-based denoising and refinement problem. Specifically, we introduced overlapped CT slices as the intermediate representations to meet the property of redundant observations in burst imaging. We performed several ablation studies to verify the effectiveness of our method and demonstrated its superiority over state-of-the-art methods through qualitative and quantitative performance evaluations.

References

- [BH07] David J Brenner and Eric J Hall. Computed tomography—an increasing source of radiation exposure. *New England Journal of Medicine*, 357(22):2277–2284, 2007.
- [CF18] Yong Chun and Jeffrey A Fessler. Deep bcd-net using identical encoding-decoding cnn structures for iterative image recovery. In *Proceedings of the IEEE Image, Video, and Multidimensional Signal Processing Workshop*, pages 1–5, 2018.
- [CZK⁺17] Hu Chen, Yi Zhang, Mannudeep K Kalra, Feng Lin, Yang Chen, Peixi Liao, Jiliu Zhou, and Ge Wang. Low-dose ct with a residual encoder-decoder convolutional neural network. *IEEE Trans. Med. Imag.*, 36(12):2524–2535, 2017.
- [CZLF19] Il Yong Chun, Xuehang Zheng, Yong Long, and Jeffrey A Fessler. Bcd-net for low-dose ct reconstruction: Acceleration, convergence, and generalization. In *Proceedings of the International Conference on Medical Image Computing and Computer-Assisted Intervention*, pages 31–40, 2019.
- [FSK⁺19] Fenglei Fan, Hongming Shan, Mannudeep K Kalra, Ramandeep Singh, Guhan Qian, Matthew Getzin, Yueyang Teng, Juergen Hahn, and Ge Wang. Quadratic autoencoder (q-ae) for low-dose ct denoising. *IEEE Trans. Med. Imag.*, 39(6):2035–2050, 2019.
- [FSU⁺05] TG Flohr, K Stierstorfer, S Ulzheimer, H Bruder, AN Primak, and CH McCollough. Image reconstruction and image quality evaluation for a 64-slice ct scanner with-flying focal spot. *Medical Physics*, 32(8):2536–2547, 2005.
- [GJN⁺18] Harshit Gupta, Kyong Hwan Jin, Ha Q Nguyen, Michael T McCann, and Michael Unser. Cnn-based projected gradient descent for consistent ct image reconstruction. *IEEE Trans. Med. Imag.*, 37(6):1440–1453, 2018.
- [GKST22] Morteza Ghahremani, Mohammad Khateri, Alejandra Sierra, and Jussi Tohka. Adversarial distortion learning for medical image denoising. *arXiv preprint arXiv:2204.14100*, 2022.
- [GY21] Jawook Gu and Jong Chul Ye. Adain-based tunable cyclegan for efficient unsupervised low-dose ct denoising. *IEEE Trans. Comput. Imaging*, 7:73–85, 2021.
- [Hsi03] Jiang Hsieh. *Computed tomography: principles, design, artifacts, and recent advances*. SPIE press, 2003.
- [HWM20] Ji He, Yongbo Wang, and Jianhua Ma. Radon inversion via deep learning. *IEEE Trans. Med. Imag.*, 39(6):2076–2087, 2020.

- [HYW⁺18] Ji He, Yan Yang, Yongbo Wang, Dong Zeng, Zhaoying Bian, Hao Zhang, Jian Sun, Zongben Xu, and Jianhua Ma. Optimizing a parameterized plug-and-play admm for iterative low-dose ct reconstruction. *IEEE Trans. Med. Imag.*, 38(2):371–382, 2018.
- [HZZS21] Zhizhong Huang, Junping Zhang, Yi Zhang, and Hongming Shan. DU-GAN: Generative adversarial networks with dual-domain u-net-based discriminators for low-dose ct denoising. *IEEE Trans. Instrum. Meas.*, 71:1–12, 2021.
- [JMFU17] Kyong Hwan Jin, Michael T McCann, Emmanuel Froustey, and Michael Unser. Deep convolutional neural network for inverse problems in imaging. *IEEE Trans. Image Process.*, 26(9):4509–4522, 2017.
- [KCY18] Eunhee Kang, Won Chang, Jaejun Yoo, and Jong Chul Ye. Deep convolutional framelet denoising for low-dose ct via wavelet residual network. *IEEE Trans. Med. Imag.*, 37(6):1358–1369, 2018.
- [KMY17] Eunhee Kang, Junhong Min, and Jong Chul Ye. A deep convolutional neural network using directional wavelets for low-dose x-ray ct reconstruction. *Medical Physics*, 44(10):e360–e375, 2017.
- [LJLW20] Tengfei Liang, Yi Jin, Yidong Li, and Tao Wang. Edcnn: Edge enhancement-based densely connected network with compound loss for low-dose ct denoising. In *Proceedings of the IEEE International Conference on Signal Processing*, volume 1, pages 193–198, 2020.
- [LLZ⁺19] Yinsheng Li, Ke Li, Chengzhu Zhang, Juan Montoya, and Guang-Hong Chen. Learning to reconstruct computed tomography images directly from sinogram data under a variety of data acquisition conditions. *IEEE Trans. Med. Imag.*, 38(10):2469–2481, 2019.
- [MCHI⁺21] Taylor R Moen, Baiyu Chen, David R Holmes III, Xinhui Duan, Zhicong Yu, Lifeng Yu, Shuai Leng, Joel G Fletcher, and Cynthia H McCollough. Low-dose ct image and projection dataset. *Medical Physics*, 48(2):902–911, 2021.
- [oPiM16] American Association of Physicists in Medicine. 2016 low dose ct grand challenge, 2016.
- [SRB⁺04] Karl Stierstorfer, Annabella Rauscher, Jan Boese, Herbert Bruder, Stefan Schaller, and Thomas Flohr. Weighted fbp—a simple approximate 3d fbp algorithm for multislice spiral ct with good dose usage for arbitrary pitch. *Physics in Medicine & Biology*, 49(11):2209, 2004.
- [SZY⁺18] Hongming Shan, Yi Zhang, Qingsong Yang, Uwe Kruger, Mannudeep K Kalra, Ling Sun, Wenxiang Cong, and Ge Wang. 3-d convolutional encoder-decoder network for low-dose ct via transfer learning from a 2-d trained network. *IEEE Trans. Med. Imag.*, 37(6):1522–1534, 2018.
- [TDV20] Matias Tassano, Julie Delon, and Thomas Veit. FastDVDnet: Towards real-time deep video denoising without flow estimation. In *Proceedings of the IEEE/CVF Conference on Computer Vision and Pattern Recognition*, pages 1354–1363, 2020.
- [TWL⁺21] Xi Tao, Yongbo Wang, Liyan Lin, Zixuan Hong, and Jianhua Ma. Learning to reconstruct ct images from the vrbp-tensor. *IEEE Trans. Med. Imag.*, 2021.
- [UEY21] Mehmet Ozan Unal, Metin Ertas, and Isa Yildirim. Self-supervised training for low-dose ct reconstruction. In *Proceedings of the IEEE International Symposium on Biomedical Imaging*, pages 69–72, 2021.
- [VSP⁺17] Ashish Vaswani, Noam Shazeer, Niki Parmar, Jakob Uszkoreit, Llion Jones, Aidan N Gomez, Lukasz Kaiser, and Illia Polosukhin. Attention is all you need. *Proceedings of the Advances in Neural Information Processing systems*, 30, 2017.
- [WFW⁺22] Dayang Wang, Fenglei Fan, Zhan Wu, Rui Liu, Fei Wang, and Hengyong Yu. Ctformer: Convolution-free token2token dilated vision transformer for low-dose ct denoising. *arXiv preprint arXiv:2202.13517*, 2022.
- [WGCM16] Tobias Würfl, Florin C Ghesu, Vincent Christlein, and Andreas Maier. Deep learning computed tomography. In *Proceedings of the International Conference on Medical Image Computing and Computer-Assisted Intervention*, pages 432–440, 2016.
- [WKEFL17] Dufan Wu, Kyungsang Kim, Georges El Fakhri, and Quanzheng Li. Iterative low-dose ct reconstruction with priors trained by artificial neural network. *IEEE Trans. Med. Imag.*, 36(12):2479–2486, 2017.

- [WME⁺06] Bruce R Whiting, Parinaz Massoumzadeh, Orville A Earl, Joseph A O’Sullivan, Donald L Snyder, and Jeffrey F Williamson. Properties of preprocessed sinogram data in x-ray computed tomography. *Medical Physics*, 33(9):3290–3303, 2006.
- [WQL⁺21] Haiyan Wu, Yanyun Qu, Shaohui Lin, Jian Zhou, Ruizhi Qiao, Zhizhong Zhang, Yuan Xie, and Lizhuang Ma. Contrastive learning for compact single image dehazing. In *Proceedings of the IEEE/CVF Conference on Computer Vision and Pattern Recognition*, pages 10551–10560, 2021.
- [XLH⁺21] Wenjun Xia, Zexin Lu, Yongqiang Huang, Zuoqiang Shi, Yan Liu, Hu Chen, Yang Chen, Jiliu Zhou, and Yi Zhang. Magic: Manifold and graph integrative convolutional network for low-dose ct reconstruction. *IEEE Trans. Med. Imag.*, 40(12):3459–3472, 2021.
- [YLM⁺21] Siqi Ye, Zhipeng Li, Michael T McCann, Yong Long, and Saiprasad Ravishankar. Unified supervised-unsupervised (super) learning for x-ray ct image reconstruction. *IEEE Trans. Med. Imag.*, 40(11):2986–3001, 2021.
- [YYZ⁺18] Qingsong Yang, Pingkun Yan, Yanbo Zhang, Hengyong Yu, Yongyi Shi, Xuanqin Mou, Mannudeep K Kalra, Yi Zhang, Ling Sun, and Ge Wang. Low-dose ct image denoising using a generative adversarial network with wasserstein distance and perceptual loss. *IEEE Trans. Med. Imag.*, 37(6):1348–1357, 2018.
- [YZL⁺19] Xiangrui Yin, Qianlong Zhao, Jin Liu, Wei Yang, Jian Yang, Guotao Quan, Yang Chen, Huazhong Shu, Limin Luo, and Jean-Louis Coatrieux. Domain progressive 3d residual convolution network to improve low-dose ct imaging. *IEEE Trans. Med. Imag.*, 38(12):2903–2913, 2019.
- [ZHS⁺21] Xiong Zhang, Zefang Han, Hong Shangguan, Xinglong Han, Xueying Cui, and Anhong Wang. Artifact and detail attention generative adversarial networks for low-dose ct denoising. *IEEE Trans. Med. Imag.*, 40(12):3901–3918, 2021.
- [ZHZ⁺21] Yikun Zhang, Dianlin Hu, Qianlong Zhao, Guotao Quan, Jin Liu, Qiegeng Liu, Yi Zhang, Gouenou Coatrieux, Yang Chen, and Hengyong Yu. Clear: comprehensive learning enabled adversarial reconstruction for subtle structure enhanced low-dose ct imaging. *IEEE Trans. Med. Imag.*, 40(11):3089–3101, 2021.
- [ZIL⁺21] Guangming Zang, Ramzi Idoughi, Rui Li, Peter Wonka, and Wolfgang Heidrich. Intratomo: self-supervised learning-based tomography via sinogram synthesis and prediction. In *Proceedings of the IEEE/CVF International Conference on Computer Vision*, pages 1960–1970, 2021.
- [ZMRB⁺22] Luis A Zavala-Mondragon, Peter Rongen, Javier Oliván Bescos, Peter HN De With, and Fons Van der Sommen. Noise reduction in ct using learned wavelet-frame shrinkage networks. *IEEE Trans. Med. Imag.*, 2022.
- [ZYL⁺21] Zhicheng Zhang, Lequan Yu, Xiaokun Liang, Wei Zhao, and Lei Xing. Transct: dual-path transformer for low dose computed tomography. In *Proceedings of the International Conference on Medical Image Computing and Computer-Assisted Intervention*, pages 55–64, 2021.